Effects of Pre-stretching and Aging Treatments on Microstructure, Mechanical Properties, and Corrosion Behavior of Spray-Formed Al-Li Alloy 2195

Yongxiao Wang, Xinwu Ma, Huakun Xi, Guoqun Zhao, Xiao Xu, and Xiaoxue Chen

In this study, different pre-stretching and aging processes were applied to spray-formed Al-Cu-Li alloy 2195. The effects of different processes on the microstructures, mechanical properties, and corrosion behaviors of the alloy were examined. The strengthening and corrosion mechanisms were investigated. The samples treated with pre-stretching and aging have higher strength than the only aged samples. However, the strength is not significantly improved with the increase in the amount of pre-stretching. The pre-stretching treatment can suppress the formations of grain boundary precipitates (GBPs) and precipitate-free zones (PFZ), and the intergranular corrosion (IGC) sensitivity of the alloy is therefore reduced. The increase in pre-stretching promotes massive precipitation of the T_1 phase, which leads to the negative shift of open-circuit potential. The over-aging treatment after pre-stretching leads to the growth of the PFZ and GBPs as well as the coarsening of the T_1 phase. These changes in microstructure cause a decrease in mechanical properties and the re-sensitivity to the IGC. Under the same pre-stretching deformation, the two-step aging treatment (110 °C/12 h + 160 °C/24 h) can result in more intensive precipitation of the T_1 phase, which enhanced the strength to a higher level. Meanwhile, the two-step aged alloy was immune to the IGC. The evolution mechanism of IGC for the alloy with different pre-stretching and aging processes was proposed based on the TEM characterization and the observation of IGC morphology.

1. Introduction

In recent years, Al-Li alloys have attracted great interest in aerospace applications due to their high specific strength, specific stiffness, and low density (Ref 1, 2). This light alloy offers significant weight reduction and fuel savings for aircraft, so it can increase the aircraft capacity and range (Ref 3, 4). The problems of poor ductility and toughness in earlier generation AL-Li alloys have been solved in the new third-generation alloys by reducing Li content (about 1 wt.%) and increasing Cu content (usually more than 3 wt.%) (Ref 4, 5). The improved Al-Li alloys have been widely used as substitutes for 2000 and 7000 series aluminum alloys in the manufacture of air and space equipment (Ref 5).

The third-generation Al-Li alloy 2195 is a kind of heat-treatable alloy. The mechanical properties of the alloy are predominated by the precipitates in the matrix. The microstructure evolution during heat treatment and its effect on mechanical properties have been reported in recent years (Ref 6-15).

Yongxiao Wang, Xinwu Ma, Guoqun Zhao, Xiao Xu, and **Xiaoxue Chen**, Key Laboratory for Liquid-Solid Structural Evolution and Processing of Materials (Ministry of Education), Shandong University, Jinan, Shandong 250061, People's Republic of China; and **Huakun Xi**, Linqu Inspection and Testing Center, Linqu, Shandong 262600, People's Republic of China. Contact e-mails: maxinwu@sdu.edu.cn and zhaogq@sdu.edu.cn.

Kim et al. (Ref 6) carried out various aging treatments on 2195 alloy plate and found that the T_1 phase is the main strengthening phase, which improved significantly the strength of the alloy. According to the nucleation mechanism of the T_1 phase, the dislocations in the matrix introduced by pre-deformation before aging can promote precipitation of this phase (Ref 7-9). Rodgers and Prangnell (Ref 10) carried out different pre-stretching on alloy 2195 and studied the quantitative relationships among the pre-stretching, microstructure, and strength increment. In addition to the pre-deformation treatment, a two-stage or multi-stage aging processes can also form the dense precipitation in the matrix. Rioja et al. (Ref 11) found that the high strength and good toughness of the Al-Li alloys 2090 and 8090 can be obtained by a two-stage aging process. Romios et al. (Ref 12) improved the mechanical properties of the Al-Li alloy 2099 and reduced its anisotropy by optimizing the multi-stage aging processes. Chen et al. (Ref 13, 14) found that the subgrain boundaries precipitation in the alloy 2195 can be suppressed by using a two-stage or multi-stage aging process, which improves the cryogenic fracture toughness significantly.

The corrosion resistance and mechanical properties of alloys are of equal importance for the application of structural parts. Many studies have documented that Al-Cu-Li alloys are highly susceptible to localized corrosion (Ref 16, 17). The localized corrosion behavior is closely related to the microstructures, especially the nature and distribution of the second phase and the characteristics of the grain boundary (Ref 16-20). It has been proved that the main mechanism of intergranular corrosion (IGC) for the Al-Cu alloys is the selective dissolutions of the copper-poor zones and precipitate-free zones (PFZ) along the grain boundaries (Ref 21). However, Rinker et al. (Ref 22) and Buchheit et al. (Ref 18) indicated that the T_1 phase in Al-Cu-Li alloy has relatively high activity and found the anodic

dissolution of precipitates at the grain or subgrain boundaries is the main cause of the interface corrosion. Donatus et al. (Ref 23) studied the intragranular corrosion behavior of 2198-T851 alloy and indicated that the alternate nanolayers formed by the parallel T_1 phase provide a path for the propagation of corrosion. Other studies have also shown that the T_1 phase inside grains promotes intragranular corrosion (Ref 24-26). In addition, some studies suggested that the corrosion sensitivity of Al-Cu-Li alloys is related to the plastic deformation degree and the internal defects of grain (Ref 27, 28). It should be noted that the dislocations, T_1 precipitate, and PFZ are closely related to each other. The dislocations can promote the precipitation of the T_1 phase, and the T_1 precipitation has competition with the formation of GBPs and PFZ (Ref 9). As mentioned earlier, the size and distribution of the T_1 phase have an important impact on the mechanical properties of the alloy. Meanwhile, the corrosion resistance of the alloy is also determined by T_1 precipitation and its interactions with dislocations and grain boundaries. The aging process has an important influence on the microstructures including precipitates, grain boundaries, and dislocations. Therefore, it is of great significance to study the microstructure evolution under different aging processes and to analyze the strengthening and corrosion mechanisms.

The spray-formed 2195 alloy is a new structural material, which is prepared based on the rapid solidification technology. During the spray forming, the molten metal is atomized into droplets and ejected at high speed. These droplets cool rapidly during the deposition process and solidified mostly before reaching the collection substrate. Therefore, the microstructure of the spray-formed billet exhibits uniform equiaxed grains instead of the dendrite structure in the casting billet. The problems such as dendritic segregation and coarse microstructure, often appearing in the casting billet, can be avoided in the spray-deposited billet (Ref 9, 29). The spray-formed alloy is required to achieve high mechanical properties through serial thermo-mechanical treatments (Ref 9). Particularly, the plates and profiles are commonly pre-stretched before aging process to reach high strength. But so far, few studies focused on the effects of pre-deformation and aging treatments on the mechanical and corrosion behavior of the spray-formed alloy 2195. In this paper, the alloy will be processed with different pre-stretching and aging parameters. The microstructure evolution of the alloy will be studied. The mechanical properties,

IGC, and electrochemical corrosion properties will be tested. The strengthening and corrosion mechanisms will be analyzed and discussed based on test results.

2. Materials and Experiments

The spray-formed billet was produced by Haoran Co., Ltd., Jiangsu, P.R. China. The chemical composition (wt.%) of the alloy was 3.72Cu, 1.06Li, 0.44Mg, 0.31Ag, 0.12Zr, and balance Al. The as-deposited alloy was hot extruded into a round bar at 470 °C with a ram speed of 1.8 mm/s. In accordance with the standard of ASTM-E8M, the tensile specimens with a gauge size of 25 × 6 mm and a thickness of 3 mm were machined from the extruded bar. The specimens were solution treated at 470 °C/1 h and 510 °C/1 h and water quenched at room temperature. Then, the solution-treated specimens were immediately pre-stretched to different deformation amounts and aged with various parameters. Figure 1 shows the schematic diagram for the whole process. The details of the pre-stretching and aging processes are shown in Table 1. The peak- and over-aging parameters listed in Table 1 were determined by hardness experiments under different aging temperatures and times. The two-step aging parameters in Table 1 were determined based on the result of the orthogonal experiment. Please refer to Appendix for the specific hardness test process and corresponding results (as shown in Fig. 16 and 17, Table 2).

The pre-stretching processes and tensile tests of the specimens were carried out on a CMT-4204 electrical testing machine. The tests were conducted at room temperature, and the tensile speed was set as 1.5 mm/min. The strain during the tests was measured by a mechanical extensometer with a gauge length of 25 mm. IGC tests were performed according to standard ASTM-G110. The sample surfaces were first mechanically polished and then cleaned in nitric acid solution. The IGC solution is a mixture of 57 g/L NaCl and 10 ml/L H_2O_2. The samples were immersed in the IGC solution at 30 ± 2 °C for 12 h. Afterward, the cross-sectional surface of IGC samples was observed by an optical microscope (OM) and scanning electron microscope (SEM) to determine the IGC mode and morphology. The electrochemical tests were carried out on a
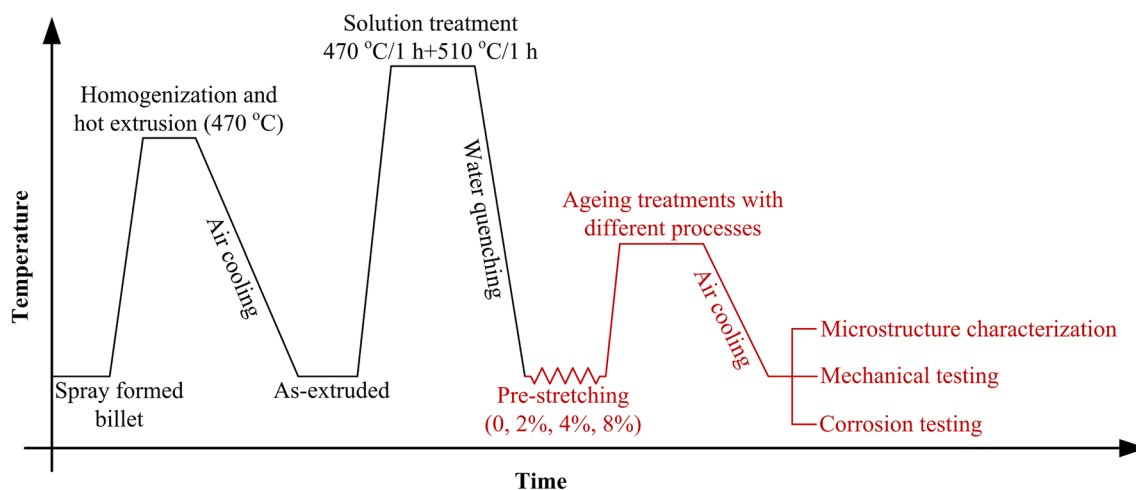

Fig. 1 Schematic diagram for the process flow of spray-formed 2195 alloy

Table 1   Pre-stretching and aging processes parameters

Temper	Processes
PA_0	Solid solution + water quench + 160 °C/30 h
PA_2	Solid solution + water quench + 2% pre-stretching + 160 °C/30 h
PA_4	Solid solution + water quench + 4% pre-stretching + 160 °C/30 h
PA_8	Solid solution + water quench + 8% pre-stretching + 160 °C/30 h
OA_4I	Solid solution + water quench + 4% pre-stretching + 170 °C/78 h
OA_4II	Solid solution + water quench + 4% pre-stretching + 180 °C/96 h
DA_4	Solid solution + water quench + 4% pre-stretching + 110 °C/12 h + 160 °C/24 h

Annotation: PA, aging to approximate peak strength; OA, over-aging; DA, duplex/two-step aging. The subscripts indicate the percent of pre-stretching before aging treatment

CHI760E electrochemical workstation, and the reference electrode is Ag/AgCl. The electrolyte was 3.5% NaCl solution. Open-circuit potential (OCP) was tested for 400 s when the electrolysis system reached stability. The temperature was maintained at 30 ± 2 °C throughout the tests.

The fracture surface and the IGC morphology were observed by an SEM (JEM-7800F). The microstructure of precipitates and grain boundary morphology was characterized by a transmission electron microscope (TEM, JEOL-2010). The samples were also characterized and analyzed by using electron backscatter diffraction (EBSD) and x-ray diffraction (XRD) techniques. Thin foils for TEM observations were firstly prepared by mechanical grinding to a thickness of 50 μm and then electrochemical polishing at − 30 °C with a double-jet electrochemical machine operated at 14 V. The electrolyte consists of 30% nitric acid and 70% methanol. The EBSD samples were prepared by using a cross-sectional polisher (IB-19510CP), and the data were analyzed using commercial software HKL CHANNEL5. The XRD samples were electropolished and then tested on a Rigaku DMAX-2500PC diffractometer with Cu-Kα radiation.

3. Results and Discussion

3.1 Microstructure and Evolution Mechanism

Figure 2 shows the TEM bright-field (BF) images of the samples PA_0, PA_2, PA_4, and PA_8. The microstructure of the sample without pre-stretching treatment (PA_0) is shown in Fig. 2(a). A lot of T_1 phases and a small quantity of θ' phase are precipitated in the matrix. The corresponding selected area electron diffraction (SAED) pattern along $< 011 >_{Al}$ direction is given in Fig. 2(e). According to the standard diffraction pattern along $< 011 >_{Al}$ zone axis presented in Fig. 2(f), it is known that the two diffraction spots at $1/3 < 220 >_{Al}$ and $2/3 < 220 >_{Al}$ positions and the streaks along $< 111 >_{Al}$ directions are formed by the diffraction of the T_1 phase. The diffraction pattern of θ' phases is not presented owing to its small volume fraction. Figure 2(b) shows the microstructure of the sample PA_2. The precipitation density of the T_1 phase increases significantly in the sample PA_2, while the size of precipitates decreases greatly. As the pre-stretching degree increases, the precipitation of the T_1 phase in samples PA_4 and PA_8 becomes denser and the precipitate size becomes smaller, as shown in Fig. 2(c) and (d). And there is less θ' phase contained in the samples PA_4 and PA_8.

Figure 3 shows the grain boundary microstructure of the samples without and with pre-stretching, i.e., samples PA_0 and PA_4. As shown in Fig. 3(a), the continuous grain boundary precipitates (GBPs) and wide PFZ appear on the grain boundaries of the sample PA_0. The grain boundary microstructure of the sample PA_4, as shown in Fig. 3(b), exhibits a narrow PFZ and small GBPs. The grain boundary microstructures of the samples PA_2 and PA_8 are similar to that of the sample PA_4. The pre-stretching before aging treatment promoted the precipitation of the T_1 phase near the grain boundaries. Due to the solute competition between the T_1 precipitations and the GBPs, the formation of PFZ and the coarsening of the GBPs were inhibited by the pre-stretching process.

Figure 4 shows the TEM images and the corresponding SAED patterns (taken in $< 110 >_{Al}$ zone axis) of the samples OA_4I, OA_4II, and DA_4. Figure 4(a) shows the microstructure of the over-aged sample OA_4I. The T_1 phase exists in the matrix, and the diffraction streaks due to the precipitates can be observed clearly in the corresponding SAED pattern. Compared with the sample PA_4, the T_1 phase size grows slightly in the over-aged sample OA_4I. As the over-aging temperature and time increase, the diameter and thickness of the T_1 phase grow up significantly as shown in Fig. 4(b). Figure 4(c) and (d) shows the microstructure of the two-step aging sample DA_4, which presents a greater T_1 precipitation density than other aged samples with the equivalent pre-stretching. The precipitation density in the sample DA_4 is higher than that in sample PA_4 and is close to that in the sample PA_8. However, the average size of the T_1 phase in the sample DA_4 is roughly the same as that in the sample PA_4. In the two-step aging condition, the solute elements such as Cu and Li diffused sufficiently during the low-temperature aging stage and segregated to the dislocations on the $\{111\}_{Al}$ planes, which accelerates nucleation and precipitation of T_1 phase in the following high-temperature aging stage (Ref 17). The precipitation density of the T_1 phase is therefore higher in the two-aged sample.

Figure 5 shows the grain boundary microstructures of the samples OA_4I, OA_4II, and DA_4. The grain boundary morphologies of the over-aged sample OA_4I are shown in Fig. 5(a) and (b). Two different microstructures of the grain boundaries can be found. As shown in Fig. 5(a), the grain boundary exhibits the continuous GBPs and narrow PFZ, while the coarse and discontinuous GBPs and wide PFZ can also be observed in the sample as shown in Fig. 5(b). The grain boundary microstructure of the sample OA_4II is shown in Fig. 5(c). Most of the grain boundaries in the serious over-aged sample exhibit the discontinuous GBPs with a size of about 200 nm
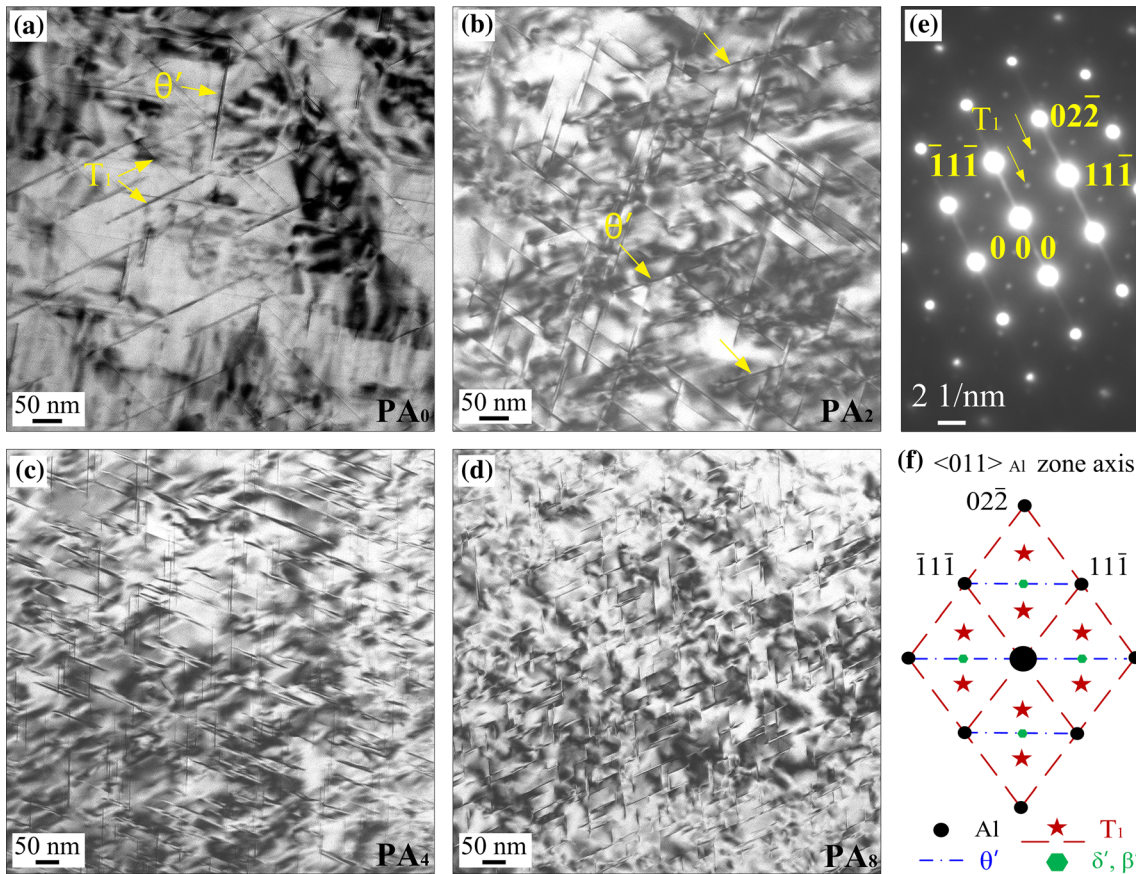
Fig. 2 TEM images of the samples with different pre-stretching and same aging treatments (taken in $< 011 >_{Al}$ zone axis): (a) BF image of the sample without pre-stretching (PA_0). (b) BF image of the sample with 2% pre-stretching (PA_2). (c) BF image of the sample with 4% pre-stretching (PA_4). (d) BF image of the sample 8% pre-stretching (PA_8). (e) SAED pattern corresponding to the BF image of the sample PA_0. (f) Standard diffraction pattern along $< 110 >$ zone axis

and the wide PFZ. Compared with the OA_4I sample, the spacing between the GBPs is larger and the PFZ along the grain boundaries also becomes wider. The grain boundary microstructure of the sample DA_4 is shown in Fig. 5(d). There is no obvious PFZ along the grain boundary, and the GBPs are small in size and exhibit interrupted shape.

The GBPs will merge and coarsen after the solute concentration in GBPs reached equilibrium with that in the areas adjacent to the grain boundaries (Ref 30). The evolution process of the GBPs can reduce the number of phases and increase their spacing. Besides, the formation of GBPs consumes the solutes in the areas adjacent to the grain boundaries, so that the strengthening phase cannot precipitate along the grain boundaries areas, which results in the formation of PFZ. The nucleation number of GBPs under different aging conditions can be predicted by Russell's model (Ref 31), as shown in formula (1):

$$N_0 = \frac{d_0 \rho_\alpha N_A}{x_\theta} \exp\left(-\frac{\Delta G^*}{kT}\right) \qquad (Eq\ 1)$$

where d_0 is the width of grain boundary, ρ_α is the molar density of the matrix phase, N_A is the Avogadro constant, x_θ is the fraction of solute atoms in the nucleation phase, ΔG^* is the Gibbs free energy for critical nucleation, T is the temperature during the nucleation process, and k is a constant. The nucleation number per unit volume for a certain GBP, i.e., N_0

is only related to the temperature T. According to Eq 1, there are more phases nucleating at the grain boundaries as the temperature increases. At the same time, the solutes at the grain boundaries will diffuse to the equilibrium state faster at higher temperatures, which will lead to merging and coarsening of the GBPs earlier. Therefore, a long time over-aging treatment at high temperature can form the large GBPs. The formation of these large GBPs consumes more solute elements at the grain boundaries, resulting in the formation of wider PFZ. In the case of two-step aging process, the solute atoms segregated to the matrix dislocations during the low-temperature aging stage and formed solute cluster or GP zones, which inhibited the flux of solutes to the grain boundaries. Besides, the slow diffusion of the solutes at the low temperature also reduced the nucleation of GBPs. Therefore, the GBPs cannot be formed massively during the low-temperature aging stage. At the high-temperature aging stage, the strengthening phase precipitated rapidly within grains and the areas adjacent to the grain boundaries, which also inhibits the growth of the GBPs and the formation of PFZ.

3.2 Mechanical Properties and Strengthening Mechanism

3.2.1 Effect of Pre-stretching and Aging Treatments on Mechanical Properties. Figure 6 shows the tensile properties of the samples with different aging treatments, including
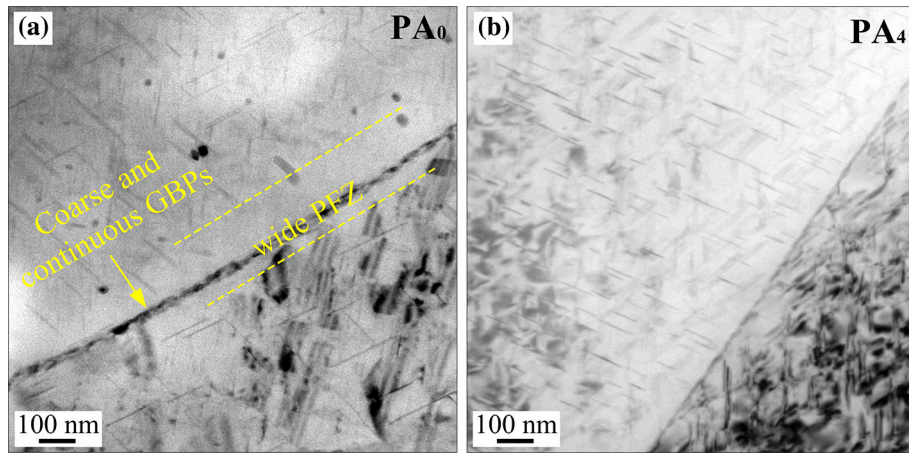
Fig. 3 Grain boundary microstructures of the aged samples with (a) no pre-stretching (PA$_0$) and (b) 4% pre-stretching (PA$_4$)
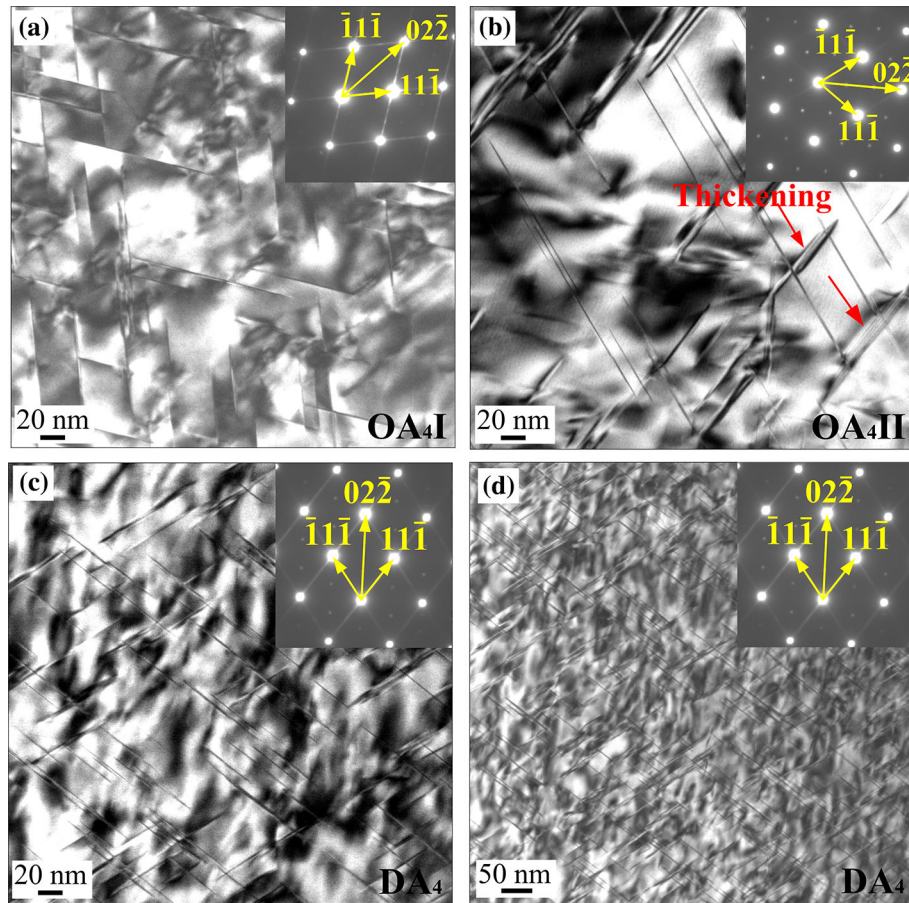

Fig. 4 TEM images and the corresponding SAED patterns of the samples with the same pre-stretching and different aging treatments (taken in $<011>_{Al}$ zone axis): (a) OA$_4$I sample; (b) OA$_4$II sample; (c) DA$_4$ sample; (d) BF image of the sample DA$_4$ at lower magnification (for comparison)

ultimate tensile strength (UTS), yield strength (YS), and elongation. The tensile properties of samples with different pre-stretching and the same aging treatment are shown in Fig. 6(a). As can be seen, the strength of the alloy can be significantly improved by the pre-stretching. The UTS of the sample without pre-stretching (PA$_0$) is 567 MPa, and the strength is increased to about 620 MPa after different degree pre-stretching (i.e., samples PA$_2$, PA$_4$, and PA$_8$). The YS is also increased from 518 MPa to more than 580 MPa after the pre-stretching. As the strength increases, the fracture elongation of the samples decreases significantly from 10.1 to 8.5%. However, as the pre-stretching degree increases, the tensile properties have no increase as much as expected. The UTS and elongation are almost unchanged as the pre-stretching increases
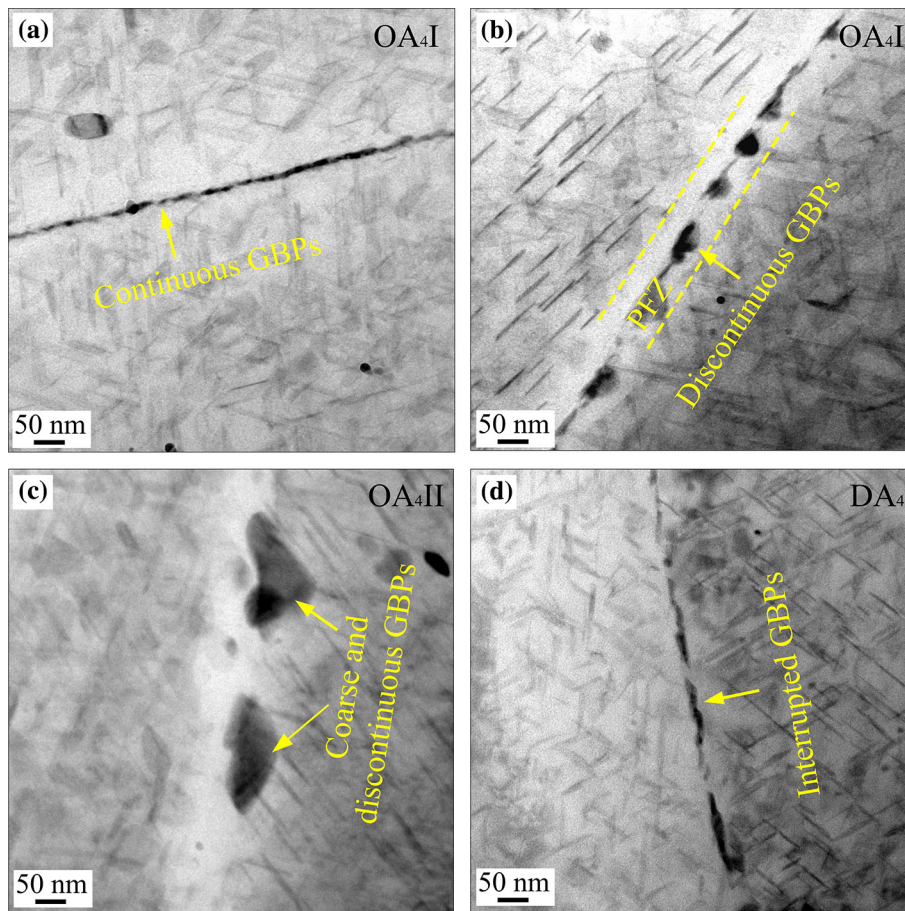
Fig. 5 Grain boundary microstructures of the samples with the same pre-stretching and different aging treatments: (a) and (b) OA_4I sample; (c) OA_4II sample; (d) DA_4 sample

from 2 to 8%. The YS of the samples is improved with the increase in pre-stretching degree. The YS of the sample with 2% pre-stretching is 580 MPa, which is increased to 610 MPa for the sample with 8% pre-stretching.

Figure 6(b) shows the tensile properties of samples aged with different parameters after the same pre-stretching. It can be seen that the UTS, YS, and elongation decrease significantly for the over-aged samples (OA_4I, OA_4II). The tensile properties of the sample OA_4II that is aged at a higher temperature for a longer time are lower than that of the sample OA_4I. The two-step-aged sample DA_4 exhibits higher YS than the single-aged sample PA_4, but the UTS of the two samples is roughly the same with each other. The YS of the sample DA_4 reaches about 602 MPa, which is close to the strength level of the sample PA_8.

Figure 7 shows the tensile fracture morphologies of different samples. The fracture surface of the sample PA_0 is shown in Fig. 7(a), exhibiting obvious intergranular fracture. Figure 7(b) shows the fracture surface of the pre-stretched and aged sample PA_4. Most area of the fracture surface shows intergranular morphology, but also a few fine dimples can be observed as marked by arrows in Fig. 7(b). As shown in Fig. 2(c) and 3(b), the dense precipitation of the T_1 phase can suppress the formation of PFZ and the growth of GBPs, which is beneficial to the strength improvement of the grain boundaries. Meanwhile, the dense T_1 phases within grains can cause dislocation aggregation and stress concentration. Therefore, the micro-

cracks may be initialed simultaneously at the grain boundaries and in grains, which results in the mixture of intergranular fracture and small dimples. The fracture morphology of the over-aged sample OA_4II as shown in Fig. 7(c) exhibits obvious intergranular morphology, and many holes and obvious secondary cracks also present in the fracture surface. For the over-aged sample, there are a lot of coarse particles distributing along the grain boundaries, as shown in Fig. 5(c). During the tensile tests, stress concentrates around the coarse particles, which triggers off crack initiation and results in the secondary cracks. The holes on the fracture surface are left by the falling particles. The fracture morphologies of the samples DA_4 are shown in Fig. 7(d). Similarly, the fracture surfaces also exhibit obvious features of intergranular fracture. All the samples show similar fracture morphology, i.e., mainly intergranular fracture, which corresponds exactly to the similar elongation to failure.

3.2.2 Strengthening Mechanism. According to previous researches (Ref 10, 32), the influence of pre-stretching on the strength of Al-Cu-Li alloy mainly depends on precipitation of the T_1 phase, and the effect of the pre-stretching itself. As shown in Fig. 2, the pre-stretching deformation before aging treatment causes more dense precipitation of the T_1 phase, which is one of the reasons for the strength improvement of the samples with pre-stretching. Besides, the pre-stretching deformation introduces a strain hardening effect in the sample, which also contributed to the strength increase. As the amount of pre-stretching increases, it is reasonable to be expected that the
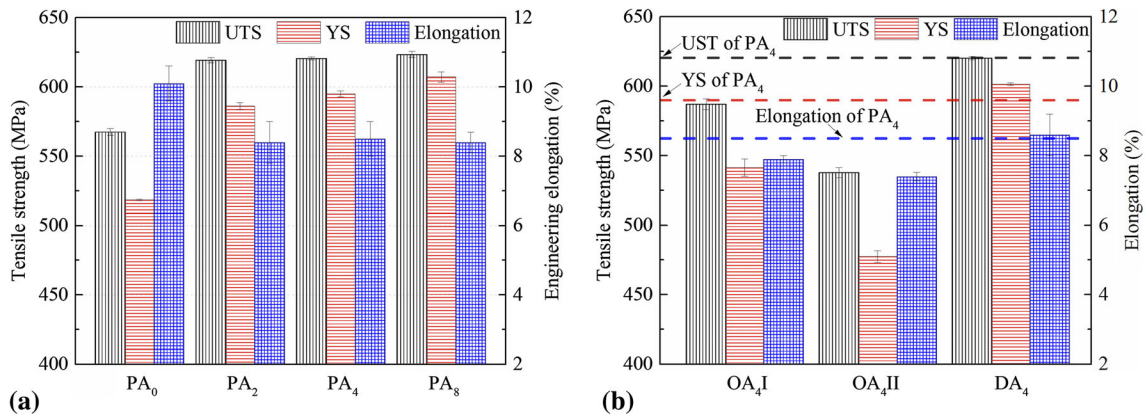
Fig. 6 Tensile properties of the samples with different processes: (a) tensile properties of the samples with different pre-stretching and the same aging treatments; (b) tensile properties of the samples with the same pre-stretching degree and different aging treatments

strength of the alloy would be increased significantly as the T_1 phase precipitates more densely. Nevertheless, the tensile properties exhibit a small difference for the samples with various pre-stretching degrees, as shown in Fig. 6(a). The analysis is as follows based on the strengthening mechanism of the T_1 phase.

The strength increment $\Delta\tau_p$ resulted from the precipitation of T_1 phase, which can be expressed by a model proposed by Nie et al. (Ref 33):

$$\Delta\tau_p = \frac{1.211 d_p}{t_p^2}\left[\frac{bf}{\Gamma}\right]^{\frac{1}{2}}\gamma_{eff}^{\frac{3}{2}} \qquad (Eq\ 2)$$

where the Burgers vector b ($b_{Al} \approx 0.286\,\text{nm}$) and the dislocation line tension Γ ($\Gamma \approx 0.5\,Gb^2$) are constants. The interfacial energy γ_{eff} after the dislocation shears the phase is about $0.107\,\text{J m}^{-2}$ (Ref 32). The phase diameter d_p, thickness t_p, and phase volume fraction f are the parameters relating to the disk-like phase T_1. The volume fraction of the precipitates depends on the equilibrium concentration of solutes in the matrix, which is determined by the aging temperature (Ref 34). And the pre-stretching degree has little effect on the volume fraction of the T_1 phase (Ref 10, 32). Besides, the thickness of the T_1 phase can be stable at the common aging temperature, and the growth in thickness will only occur during the over-aging process at high temperatures. Therefore, the phase diameter d_p is the only parameter affecting the strength increment $\Delta\tau_p$ at normal constant aging temperature, and the $\Delta\tau_p$ decreases with the phase diameter d_p. As the pre-stretching increased, the size of the T_1 phase decreased, which reduced the contribution to the strength increment. Besides, the strain hardening effect becomes stronger as the pre-stretching degree increases, which results in a greater strength increment. The opposite change between the two types of strengthening effects leads to the less significant improvement of tensile strength. For the two-step aging sample DA_4, the average size of the T_1 phase is similar to that of the sample PA_4, and the strain hardening effects are also close to each other due to the same pre-stretching degree. Therefore, for the two samples, the strength increments resulting from the T_1 phase and strain hardening are similar. However, the precipitation density in the sample DA_4 is significantly higher than that in the sample PA_4. The denser T_1 phase on the $\{111\}_{Al}$ planes has a stronger blocking effect on

the dislocations motion (Ref 17, 35), which leads to the higher strength of the sample DA_4.

The T_1 phase grows to a larger size under the over-aging condition, but its strength is lower than that of the samples with smaller precipitates. The increase in T_1 phase thickness and the decrease in precipitate density, as shown in Fig. 4, are considered to be the main cause of the decrease in strength. According to the model in Eq 2, the strength increment caused by the T_1 phase is inversely proportional to the square of the phase thickness. Therefore, the strengthening effect of the T_1 phase decreases at a quadratic exponential rate with the increase in the thickness, while the reduction of phase diameter can only increase the strengthening effect at a linear rate. A small increase in thickness can lead to a significant decrease in strength. Besides, the lower density of phases in the over-aged samples also results in the decrease in strength.

In addition, it is also required to consider the effect of the over-aging process on another important strengthening factor, i.e., strain hardening effect. The strain hardening effect would be reduced if the dislocations recovery occurs during the over-aging at high temperature for a long time, which could also lead to the decrease in strength. Figure 8 shows local misorientation maps and distributions of the samples PA_4 and OA_4II. The local misorientation difference derived from the EBSD data, which is the average misorientation of a pixel with its neighboring pixels, gives an estimate of intragranular dislocation activity. As can be seen from Fig. 8, the local misorientation distributions of the two samples are very close to each other, which indicates that dislocations activities in the over-aging and peak-aging samples are similar. Therefore, the over-aging process has little effect on the strain hardening effect resulting from the pre-stretching. It can be considered that the decrease in strength under the over-aging condition was mainly caused by the change of the T_1 phase.

3.3 Corrosion Behaviors and Mechanism

3.3.1 IGC Test and Characterization. The IGC tests were performed on the samples with different pre-stretching and aging treatments, and the cross-sectional corrosion morphologies are shown in Fig. 9. As shown in Fig. 9(a), the corrosion morphology of the sample PA_0 exhibits a general IGC feature. The serious IGC appears on the area close to the sample surface, where the grains are separated from each other
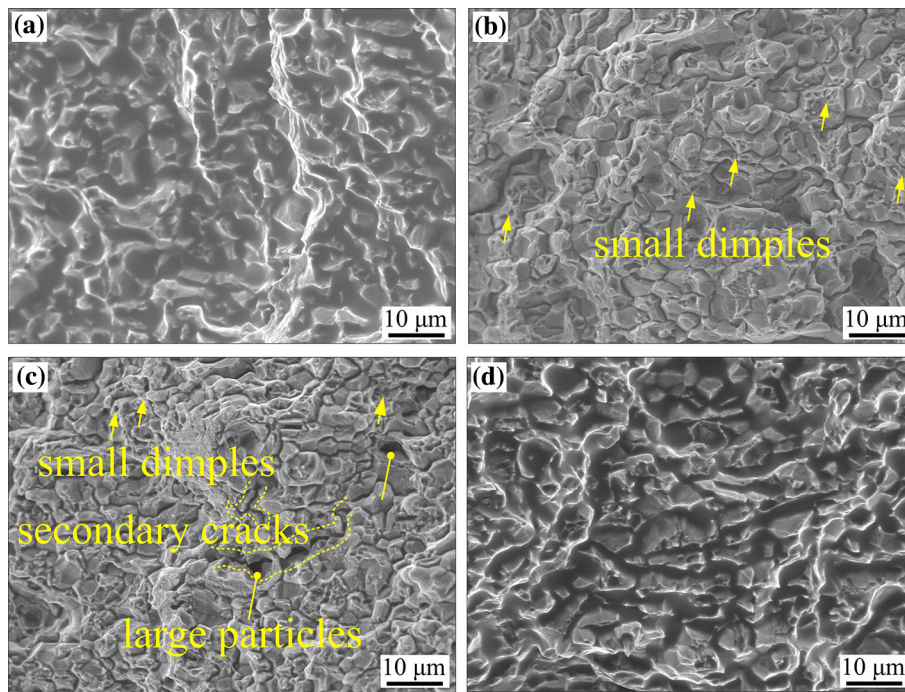
Fig. 7 Fracture surfaces of the samples with different aging treatments: (a) sample PA_0, (b) sample PA_4, (c) sample OA_4II, (d) sample DA_4

and exhibit the fragmented microstructure. Under the heavily corroded surface, there are lightly IGC morphologies extending into the deeper area, which can be observed by OM and SEM as shown in Fig. 9(b). The corrosion morphologies of samples with different pre-stretching, i.e., samples PA_2, PA_4, and PA_8, are presented in Fig. 9(c)-(e). The corrosion morphologies of the samples with pre-stretching exhibit obvious pitting features instead of the IGC. It can be considered that the pre-stretching before aging treatment can inhibit the IGC, but it will lead to the pitting.

Figure 10 shows the corrosion morphologies of the samples OA_4I, OA_4II, and DA_4. As shown in Fig. 10(a) and (b), the over-aged samples OA_4I and OA_4II show obvious IGC morphologies. Compared with the OA_4I sample, the sample OA_4II exhibits more severe IGC features, in which large areas with light IGC features can be observed below the sample surface, as shown in Fig. 10(b) and (c). The corrosion morphology of the two-step aging sample DA_4 as shown in Fig. 10(d) exhibits mainly pitting instead of the IGC. Figure 11 shows the SEM images for presenting the microstructures of the pitting clearly. The layered or stepped corrosion morphologies can be found in the pitting.

The pitting morphologies of the samples (PA_2-PA_8 and DA_4) are mainly caused by intragranular corrosion which is related to the dense T_1 phase within grains. And the microstructure of small PFZ and GBPs in the samples resulted in a small potential difference between grain interior and grain boundaries (Ref 19), which leads to low IGC sensitivity. Meanwhile, the dense T_1 inside grains promoted the intragranular corrosion. Donatus et al. (Ref 23) found that the T_1 phase inside grain can lead to the distinct nanolayers consist of parallel bands with alternating active and noble zones. During corrosion, the corrosion rate along the active layer containing the T_1 phase was faster than that along the noble layer, and the layered corrosion morphology can be left after the corrosion.

3.3.2 IGC Mechanism Analysis. Under different pre-stretching and aging processes, the 2195 Al-Cu-Li alloy exhibits two types of corrosion morphologies, i.e., IGC and pitting. The aged sample PA_0 without pre-stretching presents general IGC morphology, while the samples PA_2-PA_8 with different pre-stretching degrees are immune to IGC. In the case of a sample without pre-stretching, the T_1 phase can precipitate extensively on the grain or subgrain boundaries during the aging treatment (Ref 19, 36), which is usually accompanied by the formation of PFZ. With this type of grain boundary microstructure, the general IGC is caused by the dissolution of anodic precipitates at grain boundaries due to the lower potential of the T_1 phase with respect to that of PFZ (Ref 18, 24). The formation of PFZ and the precipitation of T_1 at grain boundaries can be suppressed by the pre-stretching deformation, which thus reduces the IGC sensitivity of the pre-stretched samples. In addition, more dense precipitation of the T_1 phase reduces the content of noble Cu in the matrix, which results in a negative shift of matrix potential. Therefore, the potential difference between the grain interior and grain boundaries was narrowed, which improved the IGC resistance.

As shown in Fig. 10, obvious IGC morphologies can be observed in the samples OA_4I and OA_4II, in which the wide PFZ and coarse particles present along the grain boundaries as shown in Fig. 5. A conclusion similar to that arrived by the sample PA_0 seems to be inferred, i.e., the precipitates at grain boundaries and the PFZ result in the IGC. However, the corrosion mechanism of the samples OA_4I and OA_4II is probably different from that of the sample PA_0.

Now suppose that the IGC is only caused by the anodic dissolution of GBPs. In this case, a more serious IGC should be caused by continuous GBPs, because they provide continuous channels for the IGC and accelerate the corrosion rate. The discontinuous GBPs formed in over-aging treatment are supposed to suppress the IGC (Ref 17, 20). However, unlike
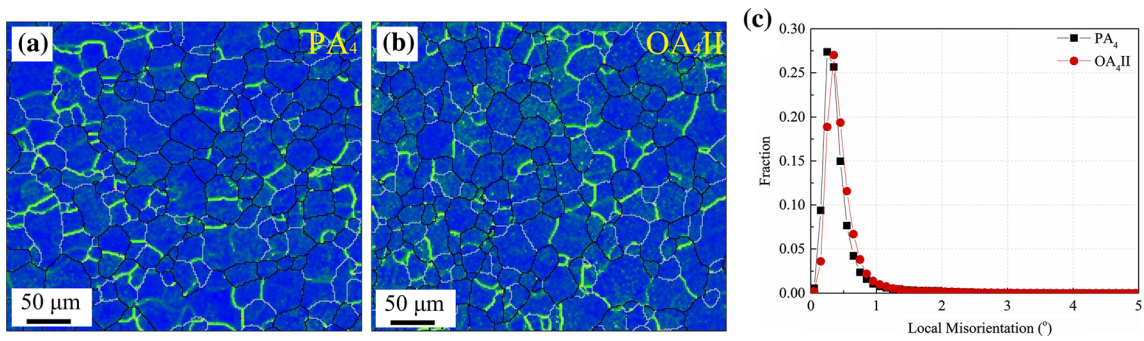
Fig. 8 Location misorientation maps of (a) peak-aging sample PA$_4$, (b) over-aging sample OA$_4$II and (c) the location misorientation distribution of the two samples
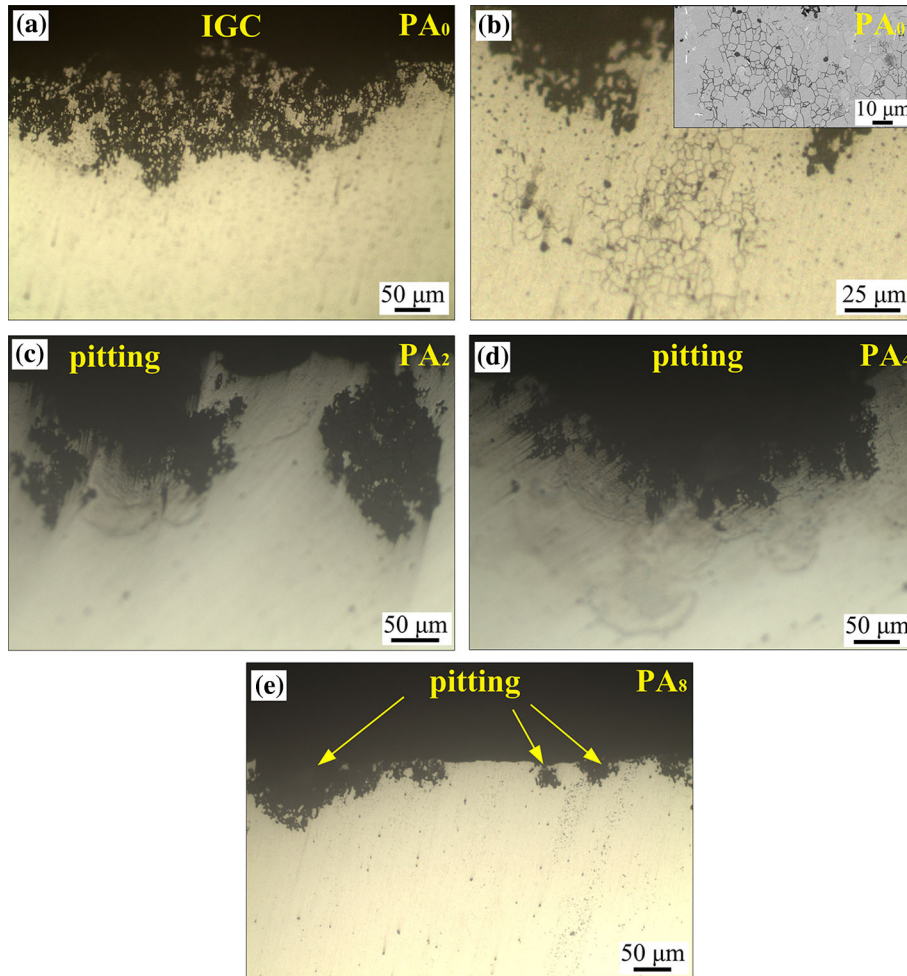

Fig. 9 Corrosion morphologies of the aged samples with different pre-stretching: (a) and (b) sample PA$_0$, (c) sample PA$_2$, (d) sample PA$_4$, (e) sample PA$_8$

the assumption above, the IGC of the over-aged samples with discontinuous GBPs is not suppressed. And the serious over-aged sample OA$_4$II with obvious discontinuous GBPs exhibits more significant IGC morphology.

Figure 12 shows the grains boundaries microstructures of sample OA$_4$I. As can be seen, there are two different types of grain boundaries in this sample. The dark-field image as shown in Fig. 12(a) exhibits a lot of T_1 phase at the grain boundary. Meanwhile, the coarse and discontinuous GBPs that are likely

to be Cu-rich phases also appear on the grain boundary, as shown in Fig. 12(b). The Cu-rich phase at the grain boundaries is noble with respect to PFZ, which acts as the cathode and leads to the preferential dissolution of the PFZ during the corrosion. Therefore, IGC can propagate rapidly through the continuous PFZ along grain boundaries. After initiation of corrosion, the two types of grain boundaries can be attacked with different corrosion mechanisms, i.e., anodic dissolutions of the T_1 precipitates and the PFZ. As the over-aging
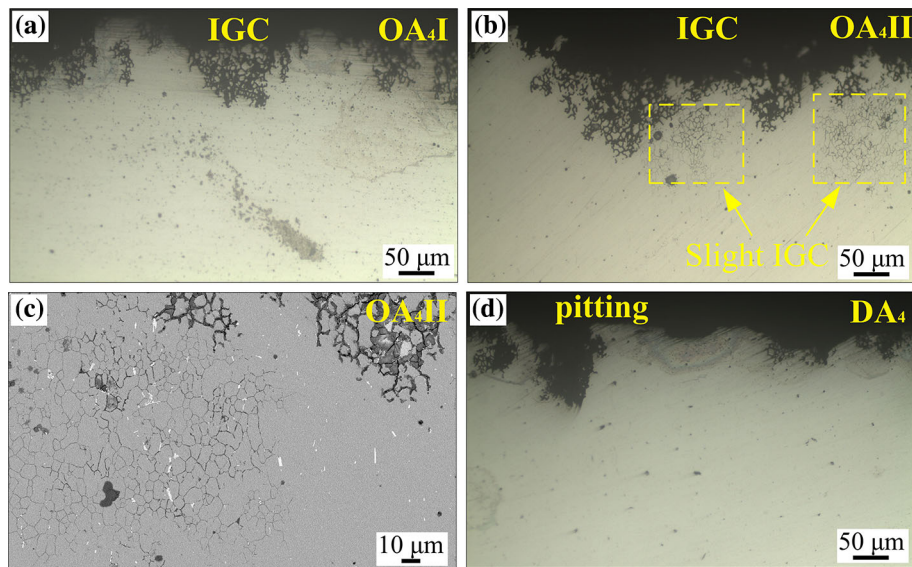
Fig. 10 Corrosion morphologies of the samples with different aging processes after the same pre-stretching: (a) sample OA_4I, (b) and (c) sample OA_4II, (d) sample DA_4
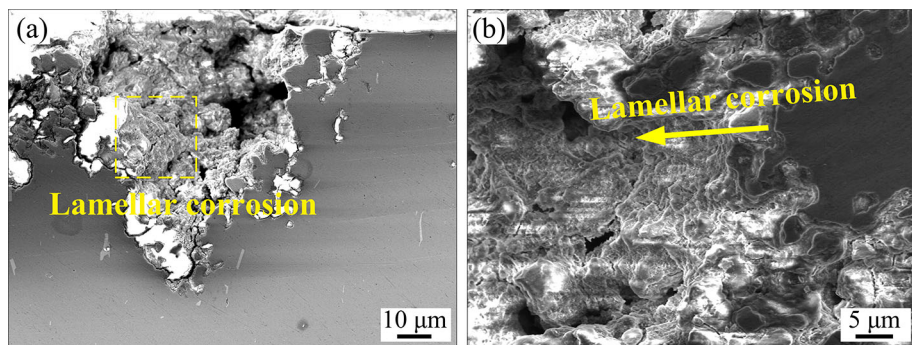

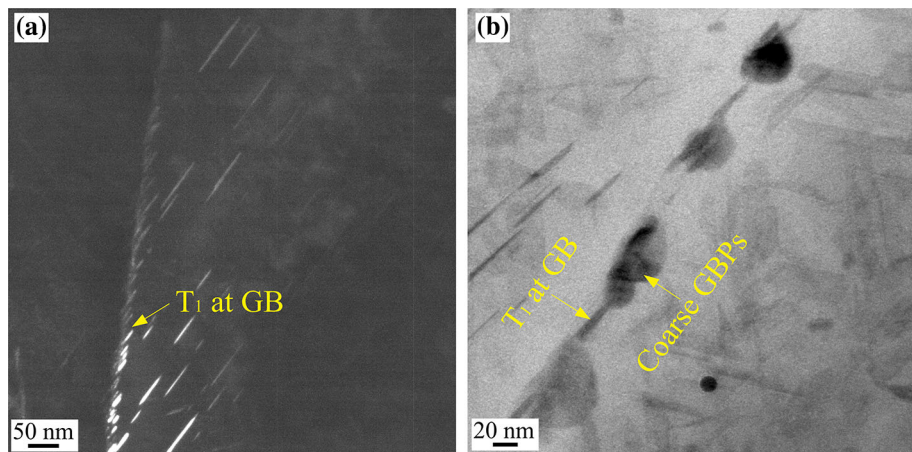**Fig. 11** Corrosion morphologies in the pitting

Fig. 12 TEM images for presenting two different types of grain boundaries in the sample OA_4I: (a) dense precipitation of T_1 phase at the grain boundary; (b) T_1 phase and coarse GBPs at the grain boundary

temperature and time increase, larger PFZ forms in sample OA_4II, and it provides more areas for IGC. Therefore, more obvious IGC can be seen in the serious over-aged sample.

There are always two arguments about the IGC mechanism of the Al-Cu-Li alloys. Some researchers argued that the IGC is mainly caused by the anodic dissolution of intergranular phases

such as T_1, T_2, T_B, and δ (Ref 17, 22, 37). The less noble phases containing active Li atoms dissolve preferentially as the sacrificial anodes during the corrosion (Ref 18, 24). However, others suggested that anodic dissolution of PFZ or Cu-depleted areas along grain boundaries is the main reason for the IGC (Ref 21, 36). In their opinion, the PFZ or Cu-depleted areas are active with respect to the GBPs. According to the analysis of Fig. 12, the two corrosion mechanisms may coexist in the aging Al-Cu-Li alloy. In recent years, researchers realized that the IGC mechanism of Al-Cu-Li alloy changes with the evolution of microstructures and compositions of the grain boundaries, which is closely related to the heat treatments and chemical compositions of the alloy itself (Ref 38, 39). Particularly, the evolutions of the GBPs and PFZ along grain boundaries have significant effects on the IGC mechanism.

According to the above discussion, the possible IGC evolution mechanism for the alloy 2195 under different pre-stretching and aging processes is given in Fig. 13. In the case of
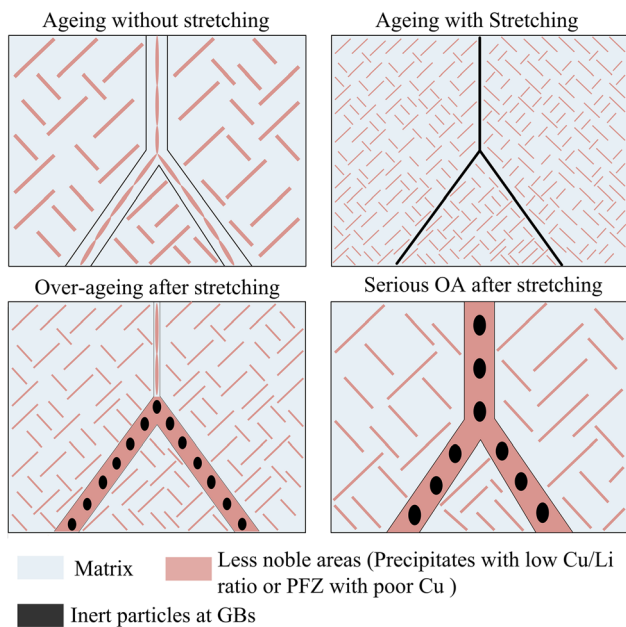

Fig. 13 Schematic diagrams showing the corrosion mechanisms for the alloy 2195 under different pre-stretching and aging conditions

the approximate peak-aged sample without pre-stretching, the IGC was mainly caused by the anodic dissolution of the continuous GBPs with high activity. After pre-stretching, the IGC of samples was suppressed due to the small PFZ and GBPs, and the sample was susceptible to intragranular corrosion owing to the dense precipitation of the T_1 phase within grains. The IGC of the over-aged samples after pre-stretching occurs through two mechanisms including the anodic dissolutions of GBPs and PFZ along grain boundaries. In the case of the serious over-aged sample, its IGC mechanism is more inclined to the anodic dissolution of PFZ owing to the larger PFZ and more discontinuous GBPs with noble Cu.

3.3.3 OCP Evolution and Mechanism Analysis. Figure 14 shows the OCP values of the samples with different pre-stretching and aging treatments. As shown in Fig. 14(a), the OCP value of the sample with higher pre-stretching shifts toward more negative value. The OCP values of the samples with different aging treatments after the same pre-stretching are shown in Fig. 14(b). As can be seen, the two over-aged samples OA_4I and OA_4II exhibit more negative OCP values than that of the peak-aged samples PA_4, and the OCP value of the serious over-aged sample OA_4II is more negative. The two-step aging sample DA_4 has roughly the same OCP value as the peak-aging sample PA_4. The negative shift of the potential usually indicates that the alloy has a greater tendency to corrode. Therefore, it can be considered that the pre-stretching before aging will increase the corrosion probability of the alloy. In the case of the same pre-stretching, the aging treatment at a higher temperature for a longer time will reduce the potential of the alloy and increase its corrosion probability.

The pre-stretching treatment can lead to an increase in the dislocation density and more precipitation of the T_1 phase. It is required to further determine the main cause of the negative shift of the OCP with the increase in pre-stretching. For this purpose, a group of reference experiments was carried out. The samples were solution treated firstly and then pre-stretched with different amounts of 0, 4%, and 8%. The OCP tests were performed on the pre-stretched samples without aging treatment. The micro-strains of the samples were also calculated by the full width at half maximum (FWHM) method based on the XRD patterns to reflect the dislocation density in the samples. (According to the model proposed by Williamson and Smallman (Ref 40), the dislocation density in the sample is proportional to the square of the micro-strain.) Before the
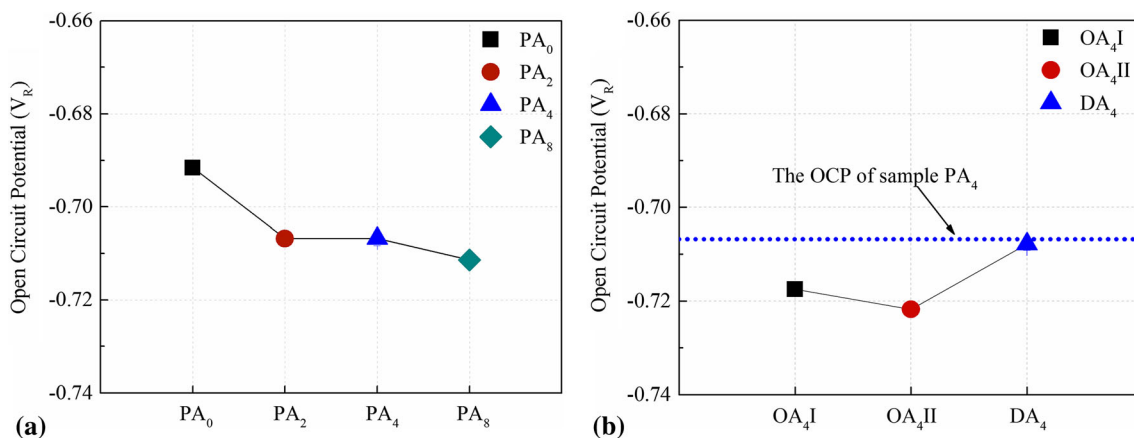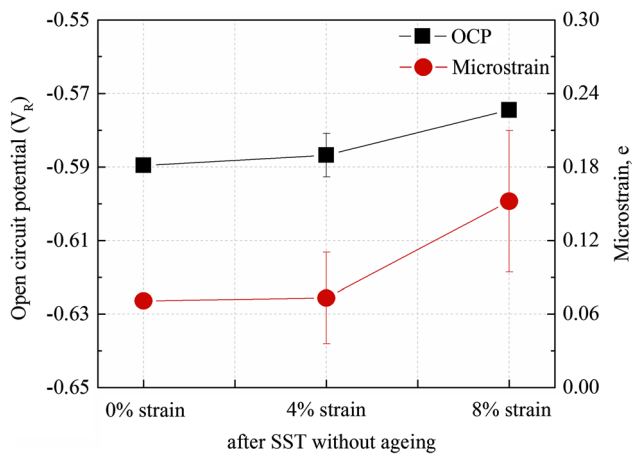

Fig. 14 OCP values of the samples with different processes: (a) OCP values of the samples with different pre-stretching and the same aging treatments; (b) OCP values of the samples with the same pre-stretching and different aging treatments

Fig. 15 OCP values and micro-strains of the samples with different pre-stretching but without aging treatment

tests, the samples were stored in the refrigerator to reduce the natural aging effect. Figure 15 shows the OCP values and micro-strains of the three samples.

As shown in Fig. 15, the results of the reference experiments show that the OCP values shift toward a positive direction with the increase in the dislocation density (micro-strain). However, as shown in Fig. 14(a), for the samples with pre-stretching and aging treatments, the increased pre-stretching results in more negative OCP value. So it can be proved that the decreased OCP values of the samples with pre-stretching and aging treatments are caused by the increase in precipitation density instead of the dislocation density. According to the analysis, it can be considered that the higher OCP value of the sample PA_0 than that of the samples PA_2-PA_8 results from the difference of precipitation density.

The pre-stretching deformation promotes more T_1 phase precipitation within the grains. On the one hand, the corrosion potential of T_1 precipitates is lower than that of the matrix, and they lead to the micro-galvanic corrosion in the grains. On the other hand, the dense precipitation of the T_1 phase can result in the reduction of Cu content in the matrix. The combined effect of the above two causes a shift of OCP toward the negative direction. Besides, more T_1 phase precipitates in the grains as the amount of pre-stretching increases, which causes the OCP to shift to a more negative potential. The strong micro-galvanic corrosion within grains causes the pitting corrosion morphology of the pre-stretched samples PA_2, PA_4, and PA_8. Under the over-aging conditions, the larger PFZ and GBPs formed at grain boundaries. The micro-galvanic corrosion occurring on the boundaries has been not negligible, which results in a further decrease in OCP and obvious IGC phenomenon in the samples OA_4I and OA_4II.

4. Conclusion

In this study, the 2195 Al-Li alloy formed by extrusion after spray deposition was subjected to different pre-stretching and aging treatments. The effects of different pre-stretching and aging on the microstructure, mechanical properties, and corrosion behaviors of the alloy were studied. The strengthen-

ing and corrosion mechanisms of the alloy were revealed. The conclusions were drawn as follows:

(1) The tensile strength of the alloy can be improved greatly by the pre-stretching before aging treatment. The growing pre-stretching can increase the precipitation density of the T_1 phase and reduce the phase size. However, the improvement of the mechanical properties is not obvious with the increase in pre-stretching. Under the same pre-stretching condition, the two-step aging treatment after pre-stretching can increase the tensile strength of the alloy to a higher level.

(2) The pre-stretching can inhibit the formation of GBPs and PFZ along grain boundaries, which reduces the IGC sensitivity of the alloy. However, the over-aging treatment after pre-stretching can lead to the coarsening of the GBPs and widening and the PFZ, which makes the sample re-sensitive to the IGC. The IGC mechanism of the alloy 2195 is the mixed anodic dissolution of PFZ and GBPs, which depends on the specific heat-treatment process. The pre-stretching can lead to negative shifts of the OCP, and the increased pre-stretching degree causes a more negative potential. The over-aging treatment after pre-stretching can also lead to negative shifts in the OCP value.

(3) In terms of the experimental results in this study, the sample aged at 160 °C/30 h after 8% pre-stretching has the highest yield strength and ultimate tensile strength. However, under the same pre-stretching deformation, a better tensile strength can be obtained by the two-step aging treatment. The IGC can be suppressed in the two-step aging sample, and its corrosion mode is pitting. The OCP of the alloy is roughly the same as that of the single-stage aged alloy.

Conflict of interest

The authors declare that they have no known competing financial interests or personal relationships that could have appeared to influence the work reported in this paper.

Appendix 1

It is known that there is a positive correlation between the hardness and strength of the alloy. Therefore, the optimal aging parameters can be determined by the simple hardness tests. The aging parameters corresponding to largest hardness value can make the alloy to reach its peak strength.

Appendix 1.1.: Determination of Single-Stage Aging Process After Pre-stretching

The samples with 4% pre-stretching were aged in the temperature range of 140-180 °C for 1-72 h. The hardness of
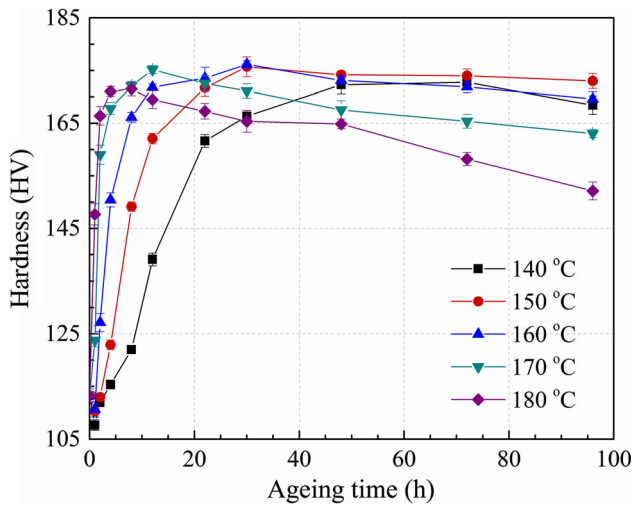
Fig. 16 Hardness curves of the samples aged at different temperatures after 4% pre-stretching

Table 2 Orthogonal experimental design and results

Test no.	A, °C	B, h	C, °C	D, h	Hardness, HV
1	100	4	150	8	149.10
2	100	8	160	12	167.18
3	100	12	170	24	168.76
4	100	24	180	48	160.00
5	110	4	160	24	172.24
6	110	8	150	48	170.30
7	110	12	180	8	167.68
8	110	24	170	12	169.04
9	120	4	170	48	168.40
10	120	8	180	24	164.02
11	120	12	150	12	163.52
12	120	24	160	8	166.48
13	130	4	180	12	167.54
14	130	8	170	8	167.36
15	130	12	160	48	168.96
16	130	24	150	24	170.88

the aged samples was measured by using a HV-1000 micro-hardness tester. The aging hardening curves at different temperatures are shown in Fig. 16. As can be seen, all the hardness values increase rapidly with aging time and then tend to be stable or decrease. The hardness of samples aged with higher temperature rises faster, and shorter time is required to reach the peak values. The hardness of the samples aged at low temperatures can keep relatively stable for a long time after reaching the peak value. However, for the samples aged at high temperature, the hardness value decreases greatly after the peak value, which is typical for the over-aging process. While the peak values for the samples aged at the temperature ranging from 150 to 170 °C are very close, the maximum hardness can be reached at 160 °C/30 h. Therefore, the single-stage peak-aging process for the samples after pre-stretching will be performed with the parameter of 160 °C/30 h.

Appendix 1.2.: Determination of Two-Stage Aging Process After Pre-stretching

The optimization for the two-stage aging process was still performed on the samples with 4% pre-stretching. There are four main factors for the two-stage aging process, including first-stage aging temperature (A), first-stage aging time (B), second-stage aging temperature (C), and the second-stage aging time (D). If there are four levels for every factor, it is required to carry out 256 experiments for the optimization if we adopt the method in the previous section. In order to reduce the number of experiments, an orthogonal experiment with four factors and four levels was selected to optimize the two-stage aging parameters. The range analysis based on the orthogonal experiment results was carried out to determine the best parameters. Table 2 shows the orthogonal experiment scheme and the experimental results.

Figure 17 shows the range analysis results of the orthogonal test. The parameters marked by the larger symbols are more beneficial to the improvement of hardness. Therefore, the optimal combination of two-stage aging parameters is $A2$, $B3$, $C2$, and $D3$. That is, the first-stage aging temperature and time are 110 °C and 12 h, and the second-stage aging temperature and time are 160 °C and 24 h, respectively.
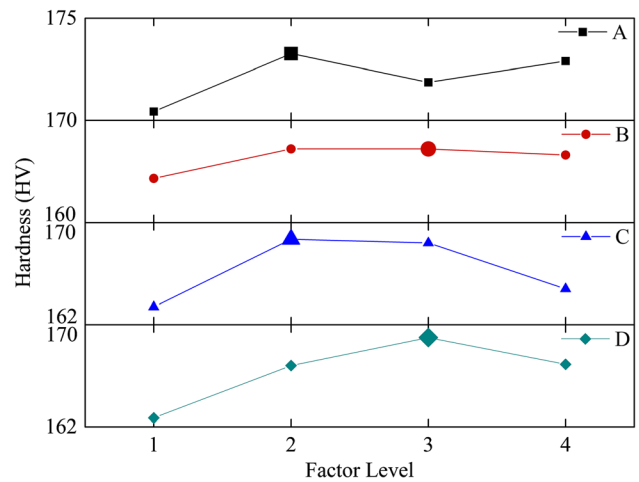

Fig. 17 Range analysis results for the orthogonal test of aging hardness

References

1. R.J. Rioja and J. Liu, The Evolution of Al-Li Base Products for Aerospace and Space Applications, *Metall. Mater. Trans. A*, 2012, **43**(9), p 3325–3337
2. J.C. Williams and J.A. Starke, Progress in Structural Materials for Aerospace Systems, *Acta Mater.*, 2003, **51**(19), p 5775–5799
3. E.A. Starke, Jr, and J.T. Staley, Application of Modern Aluminum Alloys to Aircraft, *Prog. Aerosp. Sci.*, 1996, **32**(2-3), p 131–172
4. N.E. Prasad, A.A. Gokhale, and R.J.H. Wanhill, *Aluminum-Lithium Alloys: Processing, Properties, and Applications*, Butterworth-Heinemann, Oxford, 2013
5. T. Warner, Recently-Developed Aluminium Solutions for Aerospace Applications, *Mater. Sci. Forum*, 2006, **519**, p 1271–1278
6. J.H. Kim, J.H. Jeun, H.J. Chun, Y.R. Lee, J.T. Yoo, J.H. Yoon, and H.S. Lee, Effect of Precipitates on Mechanical Properties of AA2195, *J. Alloy. Compd.*, 2016, **669**, p 187–198
7. W.A. Cassada, G.J. Shiflet, and E.A. Starke, The Effect of Plastic Deformation on Al₂CuLi (T_1) Precipitation, *Metallurg. Trans. A*, 1991, **22**(2), p 299–306
8. B.M. Gable, A.W. Zhu, A.A. Csontos, and E.A. Starke, The Role of Plastic Deformation on the Competitive Microstructural Evolution and Mechanical Properties of a Novel Al-Li-Cu-X Alloy, *J. Light Met.*, 2001, **1**(1), p 1–14

9. Y.X. Wang, G.Q. Zhao, X. Xu, X.X. Chen, and W.D. Zhang, Microstructures and Mechanical Properties of Spray Deposited 2195 Al-Cu-Li Alloy through Thermo-mechanical Processing, *Mater. Sci. Eng. A-Struct.*, 2018, **727**, p 78–89

10. B.I. Rodgers and P.B. Prangnell, Quantification of the Influence of Increased Pre-stretching on Microstructure-Strength Relationships in the Al-Cu-Li Alloy AA2195, *Acta Mater.*, 2016, **108**, p 55–67

11. R.J. Rioja, E.L. Colvin, A.K. Vasudevan, and B.A. Cheney. Aluminum Alloy Two-Step Ageing Method and Article, U.S. Patent No. 4861391, 1989

12. M. Romios, R. Tiraschi, C. Parrish, H.W. Babel, J.R. Ogren, and O.S. Es-Said, Design of Multistep Ageing Treatments of 2099 (C458) Al-Li Alloy, *J. Mater. Eng. Perform.*, 2005, **14**(5), p 641–646

13. P.S. Chen, A.K. Kuruvilla, T.W. Malone, and W.P. Stanton, The Effects of Artificial Ageing on the Microstructure and Fracture Toughness of Al-Cu-Li Alloy 2195, *J. Mater. Eng. Perform.*, 1998, **7**(5), p 682–690

14. P.S. Chen and W.P. Stanton, Artificial Effects on Cryogenic Fracture Toughness of the Main Structural Alloy for the Super Light-Weight Tank, *MRS Online Proc. Libr. Arch.*, 1998, **551**, p 285–290

15. T. Dorin, F. de Geuser, W. Lefebvre, C. Siglib, and A. Deschampset, Strengthening Mechanisms of T_1 Precipitates and Their Influence on the Plasticity of an Al-Cu-Li Alloy, *Mater. Sci. Eng. A Struct.*, 2014, **605**, p 119–126

16. Y. Ma, X. Zhou, Y. Liao, Y. Yi, H. Wu, Z. Wang, and W. Huang, Localised Corrosion in AA2099-T83 Aluminium-Lithium Alloy: the Role of Grain Orientation, *Corros. Sci.*, 2016, **107**, p 41–48

17. Y. Lin, C. Lu, C. Wei, and Z. Zheng, Effect of Ageing Treatment on Microstructures, Tensile Properties and Intergranular Corrosion Behavior of Al-Cu-Li Alloy, *Mater. Charact.*, 2018, **141**, p 163–168

18. R.G. Buchheit, J.P. Moran, and G.E. Stoner, Electrochemical Behavior of the T_1 (Al_2CuLi) Intermetallic Compound and Its Role in Localized Corrosion of Al-2% Li-3% Cu Alloys, *Corrosion*, 1994, **50**(2), p 120–130

19. J.L. Huang, J.F. Li, D.Y. Liu, R.F. Zhang, Y.L. Chen, X.H. Zhang, P.C. Ma, R.K. Gupta, and N. Birbilis, Correlation of Intergranular Corrosion Behaviour with Microstructure in Al-Cu-Li Alloy, *Corros. Sci.*, 2018, **139**, p 215–226

20. W. Yang, S. Ji, Q. Zhang, and M. Wang, Investigation of Mechanical and Corrosion Properties of an Al-Zn-Mg-Cu Alloy under Various Ageing Conditions and Interface Analysis of η′ Precipitate, *Mater. Des.*, 2015, **85**, p 752–761

21. A. Garner and D. Tromans, Direct Observation of Intergranular Corrosion in Al-4wt% Cu Alloy, *Corrosion*, 1979, **35**(2), p 55–60

22. J.G. Rinker, M. Marek, and T.H. Sanders, Microstructure, Toughness and Stress Corrosion Cracking Behavior of Aluminum Alloy 2020, *Mater. Sci. Eng.*, 1984, **64**(2), p 203–221

23. U. Donatus, M. Terada, C.R. Ospina, F.M. Queiroz, A.F.S. Bugarin, and I. Costa, On the AA2198-T851 Alloy Microstructure and Its Correlation with Localized Corrosion Behaviour, *Corros. Sci.*, 2018, **131**, p 300–309

24. J.F. Li, C.X. Li, Z.W. Peng, W.J. Chen, and Z.Q. Zheng, Corrosion Mechanism Associated with T_1 and T_2 Precipitates of Al-Cu-Li Alloys in Nacl Solution, *J. Alloy. Compd.*, 2008, **460**(1-2), p 688–693

25. J.F. Li, Z.Q. Zheng, S.C. Li, W.J. Chen, W.D. Ren, and X.S. Zhao, Simulation Study on Function Mechanism of Some Precipitates in Localized Corrosion of Al Alloys, *Corros. Sci.*, 2007, **49**(6), p 2436–2449

26. V. Proton, J. Alexis, E. Andrieu, J. Delfosse, A. Deschamps, D.G. Frédéric, M.C. Lafonta, and C. Blanc, The Influence of Artificial Ageing on The Corrosion Behaviour of a 2050 Aluminium-Copper-Lithium Alloy, *Corros. Sci.*, 2014, **80**, p 494–502

27. Y. Ma, X. Zhou, W. Huang, Y. Liao, X. Chen, X. Zhang, and G.E. Thompson, Crystallographic Defects Induced Localised Corrosion in AA2099-T8 Aluminium Alloy, *Corros. Eng. Sci. Techn.*, 2015, **50**(6), p 420–424

28. X. Zhang, X. Zhou, T. Hashimoto, J. Lindsay, O. Ciuca, C. Luo, Z. Sun, X. Zhang, and Z. Tang, The Influence of Grain Structure on the Corrosion Behaviour of 2A97-T3 Al-Cu-Li Alloy, *Corros. Sci.*, 2017, **116**, p 14–21

29. M.M. Sharma, M.F. Amateau, and T.J. Eden, Mesoscopic Structure Control of Spray Formed High Strength Al-Zn-Mg-Cu Alloys, *Acta Mater.*, 2005, **53**(10), p 2919–2924

30. H. Jiang and R.G. Faulkner, Modelling of Grain Boundary Segregation, Precipitation and Precipitate-Free Zones of High Strength Aluminium Alloys-I, *The Model, Acta Mater.*, 1996, **44**(5), p 1857–1864

31. K.C. Russell, Grain Boundary Nucleation Kinetics, *Acta Metall.*, 1969, **17**(8), p 1123–1131

32. T. Dorin, A. Deschamps, F.D. Geuser, and C. Sigli, Quantification and Modelling of the Microstructure/Strength Relationship by Tailoring the Morphological Parameters of the T_1 Phase in an Al-Cu-Li Alloy, *Acta Mater.*, 2014, **75**, p 134–146

33. J.F. Nie and B.C. Muddle, Microstructural Design of High-Strength Aluminum Alloys, *J. Phase Equilib.*, 1998, **19**(6), p 543–551

34. H.R. Shercliff and M.F. Ashby, A Process Model for Age Hardening of Aluminium Alloys-I, the model, *Acta Metall. Mater.*, 1990, **38**(10), p 1789–1802

35. J. Xu, Y. Deng, J. Chen, and X. Gao, Effect of Ageing Treatments on the Precipitation Behavior and Mechanical Properties of Al-Cu-Li Alloys, *Mater. Sci. A Struct.*, 2020, **773**, p 138885

36. C. Kumai, J. Kusinski, G. Thomas, and T.M. Devine, Influence of Ageing at 200 C on the Corrosion Resistance of Al-Li and Al-Li-Cu Alloys, *Corrosion*, 1989, **45**(4), p 294–304

37. Q. Liu, R.H. Zhu, D.Y. Liu, Y. Xu, J.F. Li, Y.L. Chen, X.H. Zhang, and Z.Q. Zheng, Correlation between Artificial Ageing and Intergranular Corrosion Sensitivity of a New Al-Cu-Li Alloy Sheet, *Mater. Corros.*, 2017, **68**(1), p 65–76

38. Y. Yan, L. Peguet, O. Gharbi, A. Deschamps, C.R. Hutchinson, S.K. Kairy, and N. Birbilis, On the Corrosion, Electrochemistry and Microstructure of Al-Cu-Li Alloy AA2050 as a Function of Ageing, *Materialia*, 2018, **1**, p 25–36

39. B.J. Connolly and J.R. Scully, Corrosion Cracking Susceptibility in Al-Li-Cu Alloys 2090 and 2096 as a Function of Isothermal Ageing Time, *Scripta Mater.*, 2000, **42**(11), p 1039–1045

40. G.K. Williamson and R.E. Smallman, III, Dislocation Densities in Some Annealed and Cold-Worked Metals from Measurements on the X-ray Debye-Scherrer Spectrum, *Philos. Mag.*, 1956, **1**(1), p 34–46